# Cyclotron resonance in tellurium. II. $\vec{B} \perp \vec{c}$

Michael von Ortenberg* and Kenneth J. Button
*Francis Bitter National Magnet Laboratory, † Massachusetts Institute of Technology, Cambridge, Massachusetts 02139*
(Received 3 December 1976)

We present the results of a detailed experimental and theoretical study of the submillimeter cyclotron resonance of holes in tellurium for the external magnetic field orientation perpendicular to the trigonal crystal axis. The comparison of experiment and theory considers not only peak positions and transition energies, but also line intensities and matrix elements. Four different $\vec{k}\cdot\vec{p}$ models are discussed with reference to the experimental results.

## I. INTRODUCTION

There has been a persistent effort during the past few years to elucidate valence-band structure of tellurium as shown in references[1-14] and references therein. Magneto-optical experiments provided sufficient data to establish the competing parameter sets for the $\vec{k}\cdot\vec{p}$ model. All of these models lead to the fundamental "dumbbell structure," but they differ in their higher-order terms and also in the values of their constant factors. Four years ago, we performed a detailed experimental and theoretical analysis of the temperature dependence of the submillimeter cyclotron resonance spectra for the special case of orientation of the external magnetic field $\vec{B}$, parallel to the $c$ axis, that is, trigonal crystal axis (Cyclotron resonance in tellurium, hereafter referred to as I)[9] in an effort to distinguish among the different models. This investigation was based on the comparison of the theoretically and experimentally determined transition energies for cyclotron-resonance absorption. Because of the special choice of the external magnetic field orientation, the magnetic-field-dependent part of the state function and, hence the transition matrix element determining the absorption intensity was independent of the various models. For any other field orientation relative to the crystal symmetry the eigenfunction is very sensitive to specific parameters of the model.

The principal objective of the present study was, therefore, to investigate the cyclotron resonance of holes in tellurium for the external magnetic field perpendicular to the crystal symmetry axis. Preliminary results have been reported at conferences.[10-12]

In Sec. II of the present paper we give an outline of the theory for the $\vec{k}\cdot\vec{p}$ Hamiltonian. We calculate both the energy eigenvalues and wave functions numerically under special consideration of the nonparabolic influence of the wave vector parallel to the magnetic field. From the transition energies and the matrix elements the absorption constant is calculated using Kubo's formula.[15] In Sec. III we present the experimental results and discuss in detail the experimentally found temperature shift of the peak position and the temperature variation of the linewidth in connection with the theoretical results. Finally we compare the experimental data with the absorption intensity determined by the matrix elements.

## II. THEORY

### A. $\vec{k}\cdot\vec{p}$ Hamiltonian

Tellurium is an elemental semiconductor which crystallizes in trigonal symmetry. The symmetry of the point group is reflected in the energy-wave number relation of the valence bands: there is a strong anisotropy of the $E(k)$ relations of the valence bands for the wave vectors parallel and perpendicular to the trigonal axis as expressed in the $2\times 2$ Hamiltonian[1]

$$\mathcal{H}=\begin{pmatrix} 2a+bk_z^2+(c+f)k_\perp^2+(d+g)k_\perp^4+ek_\perp^2k_z^2 & -h^{1/2}k \\ -h^{1/2}k_z & bk_z^2+(c-f)k_\perp^2+(d-g)k_\perp^4+ek_\perp^2k_z^2 \end{pmatrix}, \tag{1}$$

where

$$k_\perp^2=k_x^2+k_y^2.$$

### B. Energy levels and eigenfunctions

Here $k_z$ and $k_\perp$ characterize the wave vector parallel and perpendicular to the trigonal axis,

TABLE I. Coefficients of the different parameter sets for the $\vec{k}\cdot\vec{p}$ model of the upper valence bands in tellurium.

$$E(\vec{k}) = a + bk_z^2 + ck_\perp^2 + dk_\perp^4 + ek_z^2k_\perp^2 + [(a + fk_\perp^2 + gk_\perp^4)^2 + hk_z^2]^{1/2}$$

$$k_\perp^2 = k_x^2 + k_y^2$$

| Parameter | Model W1 | Model W2 | Model J | Model C |
|---|---|---|---|---|
| $a$ | 0.063 15 eV | 0.063 15 eV | 0.063 15 eV | 0.063 eV |
| $b$ | $-10.0\hbar^2/2m_0$ | $-10.1\hbar^2/2m_0$ | $-10.5\hbar^2/2m_0$ | $-11.13\hbar^2/2m_0$ |
| $c$ | $-5.55\hbar^2/2m_0$ | $-9.95\hbar^2/2m_0$ | $-6.82\hbar^2/2m_0$ | $-9.26\hbar^2/2m_0$ |
| $d$ | $0.3\times10^{-28}$ eV cm$^4$ | $1.1\times10^{-28}$ eV cm$^4$ | $0.63\times10^{-28}$ eV cm$^4$ | 0 |
| $e$ | $0.2\times10^{-28}$ eV cm$^4$ | 0 | 0 | 0 |
| $f$ | $-5.55\hbar^2/2m_0$ | 0 | $-3.46\hbar^2/2m_0$ | 0 |
| $g$ | 0 | 0 | $-0.42\times10^{-29}$ eV cm$^4$ | 0 |
| $h$ | $6.18\times10^{-16}$ (eV cm)$^2$ | $6.25\times10^{-16}$ (eV cm)$^2$ | $6.76\times10^{-16}$ (eV cm)$^2$ | $6.92\times10^{-16}$ (eV cm)$^2$ |

respectively. The coefficients are related to interband matrix elements whose numerical values differ in the numerous established models. We discuss in this paper four different parameter sets of the $\vec{k}\cdot\vec{p}$ model which have been established from experimental data on cyclotron resonance. The different models are abreviated by W1,[1] W2,[2] J,[3] and C,[6] where W1,[1] W2,[2] J,[3] and C,[6] stand for models described in Refs. 1, 2, 3, and 6, respectively. The corresponding parameter sets are listed in Table I. A detailed discussion of models W1, W2, and J is given in I.[9] Model C has the least number of parameters and has been suggested by Couder *et al.*[6] Although model W2 has already been ruled out to be realistic in I, we have still included this model in our theoretical investigation for completeness. To demonstrate the differences in the four models more directly we have plotted in the left and right part of Fig. 1 the energy–wave-number relations for the two different planes in $k$ space: $k_\perp = 0$ and $k_z = 2\times10^6$ cm$^{-1}$, respectively. The latter corresponds to the cut through the camel-back maximum in the left part of the figure.

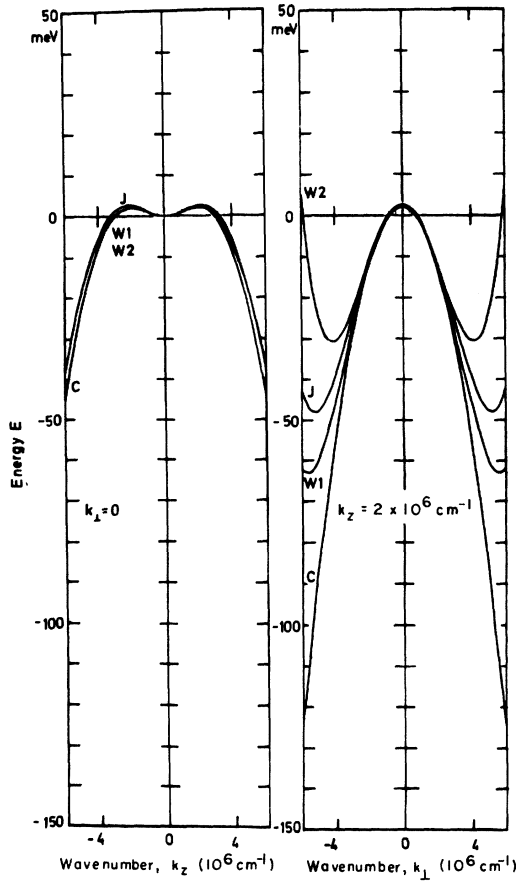


FIG. 1. For all of the discussed four models W1 (Ref. 1), W2 (Ref. 2), J (Ref. 3) and C (Ref. 6) the energy–wave-number relation of the upper valence band in tellurium exhibits the famous "camel-back" structure as shown in the left-hand part. In the right-hand part the different influence of the $k^4$ terms is demonstrated.

Because of the strong anisotropy of the Hamiltonian of Eq. (1) the energy spectra and corresponding eigenfunctions of the valence bands in the presence of an external magnetic field differ considerably depending on the orientation of the crystal relative to the field direction.

For the external magnetic field perpendicular to the symmetry axis of the crystal ($\vec{B}\perp\vec{c}, \vec{B}\parallel\vec{y}$) we have to replace the wave vectors $k_x$ and $k_z$ in Eq. (1) by the following operators:

$$k_x = ia^+ - a^-/\lambda\sqrt{2}\,, \quad k_y = a^+ + a^-/\lambda\sqrt{2} \tag{2}$$

does not commute with the oscillator-number operator $a^-a^+$. As a consequence of this, the eigenfunction of $\psi$ is not a pure oscillator function as $\vec{B}\parallel\vec{c}$, but a linear combination of oscillator functions with different oscillator quantum numbers. Since the parity operator still commutes with $\mathcal{H}$, the eigenfunctions will split into two sets of even and odd parity:

$$\psi^+ = \sum_{N=0}^{\infty}(a_{2N}\phi_{2N}u_4 + b_{2N+1}\phi_{2N+1}u_5)\,, \tag{3}$$

$$\psi^- = \sum_{N=0}^{\infty}(a_{2N+1}\phi_{2N+1}u_4 + b_{2N}\phi_{2N}u_5)\,. \tag{4}$$

Here $u_4$ and $u_5$ are the state functions of the $H_4$ and $H_5$ band, respectively. The coefficients $a_N$ and $b_N$ depend explicitly on the detailed parameter set of the investigated model. This means that for the orientation of an external magnetic field perpendicular to the symmetry axis of tellurium any magneto-optical experiment provides a useful tool for the study of the model-dependent eigenfunctions.

There have been various attempts for the diagonalization of the Hamiltonian of Eq. (1) for a magnetic field $\vec{B} \perp \vec{c}$.[1-4,6] All these calculations, however, were performed in the limit $k_y = 0$. Consequently no nonparabolic effects in $k_y$ could be investigated.

We computed both the energy eigenfunctions and eigenvalues of $\mathcal{H}$ as a function of the magnetic field intensity and the $k$ vector parallel to the magnetic field for the four discussed models. Because of the limited space within this paper we shall demonstrate the general features of our theoretical results only in model W1. The differences of line positions and temperature dependence, however, of all the different models is given in detail. In Fig. 2 we represent typical numerical results as calculated in model W1. In the upper part of this figure we have plotted the energies of the five lowest Landau levels of holes in tellurium as a function of the magnetic field intensity perpendicular to the trigonal axis. The solid and broken curves represent the results for two different values of the wave vector parallel to the magnetic field, namely $k_x = 0$ and $k_x = 0.6\, k_M$, where $k_M$ has the value of about $2 \times 10^6$ cm$^{-1}$ and corresponds to the abscissa of the camel-back extrema in the left part of Fig. 1. The Landau levels are labeled by the Landau quantum number and the parity symbol. In addition to that, the analog of the classical orbit is indicated. At low magnetic field intensities, the energy levels are doubly degenerated. At high magnetic field intensities, this degeneracy is lifted by magnetic breakdown of the two merging ellipsoids in $k$ space. The vertical lines indicate the magnetic field position of the optical transitions induced by 337- and 220-$\mu$m wavelength radiation. In the middle part we have plotted the corresponding transition energies as a function of the magnetic field intensity. In all models but model C the transition energies are shifted to higher magnetic field intensity with increasing value of the $k$ vector parallel to the magnetic field $k_x$. This means that generally with increasing temperature and, hence, population of states with nonzero $k_x$ vector for fixed radiation energies, the transition is shifted to higher magnetic field intensities.

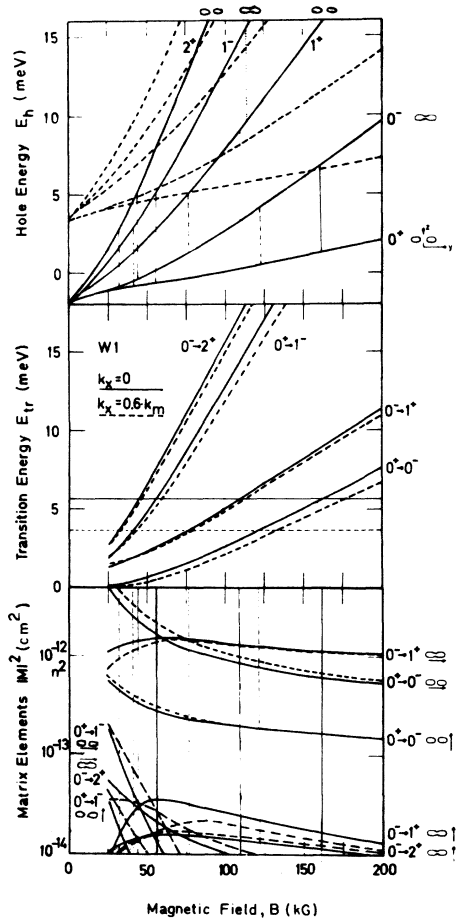


FIG. 2. Landau levels, corresponding transition energies, and transition-matrix elements of holes in tellurium as a function of the magnetic field intensity perpendicular to the $c$ axis as calculated in model W1 (Ref. 1). The difference of the solid and broken curves demonstrates the influence of the nonparabolicity due to the wave vector parallel to the magnetic field.

In Fig. 3 we illustrate this effect of nonparabolicity. We have plotted the Landau levels in model W1 for two fixed magnetic field intensities as a function of the $k$ vector parallel to the magnetic field. The energy separation of the different Landau levels decreases with increasing values of $k_x$. In the lower part of Fig. 2 we have plotted the square of the corresponding transition-matrix element of the coordinate of the charged particle. For the given orientation of the magnetic field there are two relevant favored orientations of the position operator, namely, parallel and perpendicular to the $c$ axis. With the knowledge of the transition energies and the matrix elements the imaginary part of the dielectric tensor components can be calculated from Kubo's formula.[15] Using the approximations and notations of Sec. II, the imaginary part of the dielectric tensor components $\epsilon_{xx}$ and $\epsilon_{yy}$ are given by

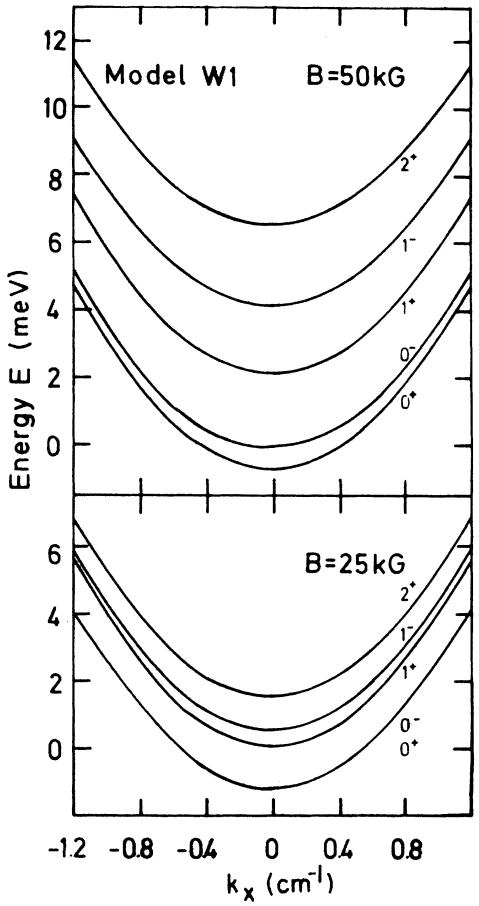


FIG. 3. Dispersion relation of the lowest Landau levels of holes in tellurium for fixed magnetic field perpendicular to the $c$ axis is strongly nonparabolic as a function of the wave vector parallel to the magnetic field orientation.

$$\mathrm{Im}(\epsilon_{xx}) = \frac{e^2\Gamma}{\epsilon_0(\hbar\omega)^2 V} \times \sum_{\alpha,\alpha'} \frac{[f(E_\alpha) - f(E_{\alpha'})](E_{\alpha'} - E_\alpha)^2 |r_{y\alpha\alpha'}|^2}{[\hbar\omega - (E_{\alpha'} - E_\alpha)]^2 + \Gamma^2}, \tag{5}$$

$$\mathrm{Im}(\epsilon_{yy}) = \frac{e^2\Gamma}{\epsilon_0(\hbar\omega)^2 V} \times \sum_{\alpha,\alpha'} \frac{[f(E_\alpha) - f(E_{\alpha'})](E_{\alpha'} - E_\alpha)^2 |r_{z\alpha\alpha'}|^2}{[\hbar\omega - (E_{\alpha'} - E_\alpha)]^2 + \Gamma^2}. \tag{6}$$

Here $e$ is the elementary charge; $\epsilon_0$, the permittivity of vacuum; $\hbar$, the reduced Planck's constant; $\omega$, the radiation frequency; $V$, the normalization volume; $f(E)$, the Fermi function; and $\Gamma$, the damping constant, which is assumed to be independent of all parameters but the temperature. $\alpha$ represents a complete set of quantum numbers of the two-dimensional eigenvectors of the Hamiltonian of Eq. (1). The summation includes therefore explicitly the integration over $k_x$ giving rise to a temperature-dependent resonance shift caused by nonparabolicity.

### C. Absorption constant

The complete dielectric tensor of tellurium oriented with its trigonal axis parallel to the $z$ direction and the magnetic field parallel to the $x$ axis can be written as

$$\epsilon_{ij} = \begin{pmatrix} \epsilon_{xx} & 0 & 0 \\ 0 & \epsilon_{yy} & \epsilon_{yz} \\ 0 & -\epsilon_{yz} & \epsilon_{zz} \end{pmatrix}. \tag{7}$$

In the Faraday configuration the complex refractive index $N_{1/2}$ of the two normal modes is given by

$$N_{1/2}^2 = \tfrac{1}{2}(\epsilon_{zz} + \epsilon_{yy}) \pm [\tfrac{1}{4}(\epsilon_{zz} - \epsilon_{yy})^2 - \epsilon_{yz}^2]^{1/2}. \tag{8}$$

Because of the strong anisotropy of the lattice part of the dielectric function[16]

$$\epsilon_{zz}^l = \epsilon_{\parallel}^l = 54, \quad \epsilon_{yy}^l = \epsilon_{xx}^l = \epsilon_{\perp}^l = 33, \tag{9}$$

for low carrier concentration Eq. (8) can be reduced to

$$N_{\perp}^2 \approx \epsilon_{yy}^l + i\,\mathrm{Im}(\epsilon_{yy}^l), \tag{10}$$

$$N_{\parallel}^2 \approx \epsilon_{zz}^l + i\,\mathrm{Im}(\epsilon_{zz}^l). \tag{11}$$

Here $N_{\parallel}$ and $N_{\perp}$ are the refractive indices of the two different normal modes whose polarization of the electric field vector is, to good approximation, parallel and perpendicular to the trigonal axis, respectively.

From Eqs. (10) and (11) we derive directly for the absorption constant for radiation of vacuum wavelength $\lambda$:

$$K_{\perp} \approx (2\pi/\lambda)\,\mathrm{Im}(\epsilon_{yy})/(\epsilon_{\perp}^l)^{1/2}, \tag{12}$$

$$K_{\parallel} \approx (2\pi/\lambda)\,\mathrm{Im}(\epsilon_{zz})/(\epsilon_{\parallel}^l)^{1/2}. \tag{13}$$

In Fig. 4 we have plotted from Eqs. (12) and (13) the calculated absorption constant of 220-$\mu m$ wavelength radiation in tellurium as a function of the magnetic field intensity perpendicular to the trigonal axis for both normal modes in model W1. As parameters we have chosen different temperatures and temperature-dependent values of the damping constant $\Gamma(T)$ corresponding to the experimental situation. The considered four different optical transitions produce four different absorption lines whose intensity is not only determined by the matrix element, but also by the

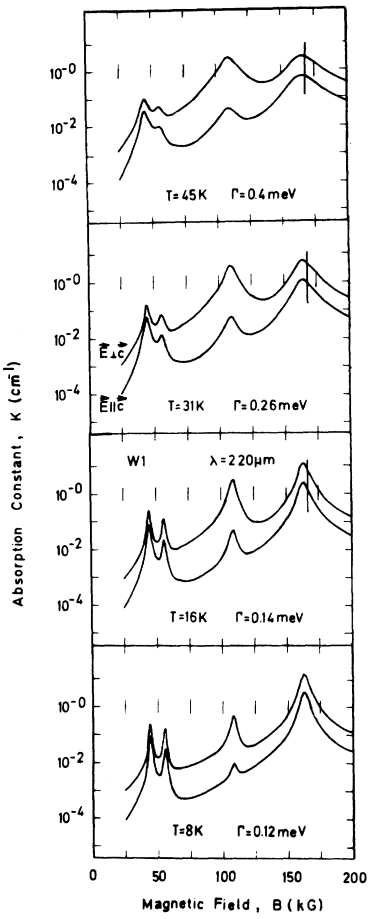


FIG. 4. Absorption constant of 220-$\mu$m wavelength radiation in tellurium as a function of the magnetic field intensity perpendicular to the $c$ axis as calculated in model W1 (Ref. 1) for different values of the temperature and temperature-dependent damping parameter $\Gamma$.

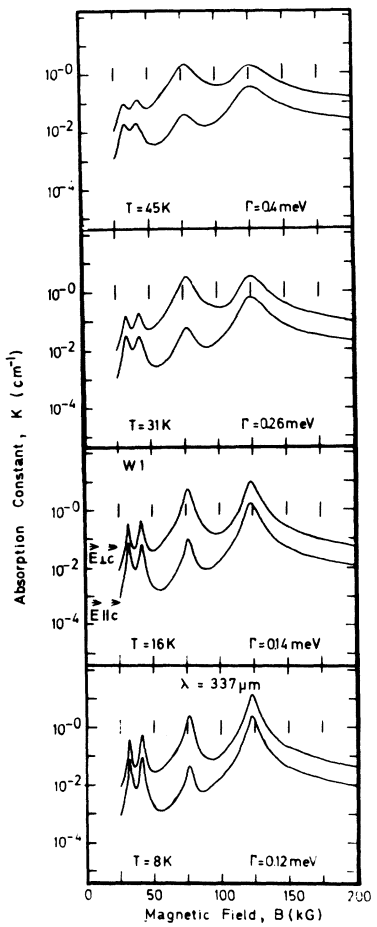


FIG. 5. Absorption constant of 337-$\mu$m wavelength radiation in tellurium as a function of the magnetic field intensity perpendicular to the $c$ axis as calculated in model W1 (Ref. 1) for different values of the temperature and temperature-dependent damping parameter $\Gamma$. Due to the strong anisotropy there are pronounced differences for the polarization of the electric vector parallel and perpendicular to the $c$ axis.

thermodynamic occupation of the involved states. The strong influence of the occupation probability is demonstrated by the strong increase of the low-field line and the line at about 100 kG. Both transitions do not start from the ground level, but from the first excited energy state $0^-$. At low temperatures this level is consequently less populated and its contribution to the absorption is only very small. At elevated temperatures, however, the $0^- 1^+$ transition is dominant because of its strong matrix element and sufficient thermal occupation of the initial state.

In Fig. 5 we have plotted the corresponding results for the absorption of the 337-$\mu$m wavelength radiation of the hydrogen-cyanide laser. The temperature dependence of the line intensity is quite analogous to the case with 220-$\mu$m wavelength radiation.

Although in all models the spectra of the absorption constant exhibit roughly the same structure, the line positions differ in detail. In particular, the dependence of the peak position as a function of temperature is a well-known tool to investigate the quality of the models. The detailed discussion of these effects will be given in connection with the experimental results in Sec. III.

## III. EXPERIMENTAL RESULTS AND DISCUSSION

### A. Experimental arrangement

We measured the submillimeter magneto-optical transmission of 220- and 337-$\mu$m wavelength radiation through pure tellurium samples ($p < 4.10^{13}$ cm$^{-3}$) as a function of the magnetic field intensity perpendicular to the trigonal axis in the Faraday configuration. The experimental setup uses a sub-

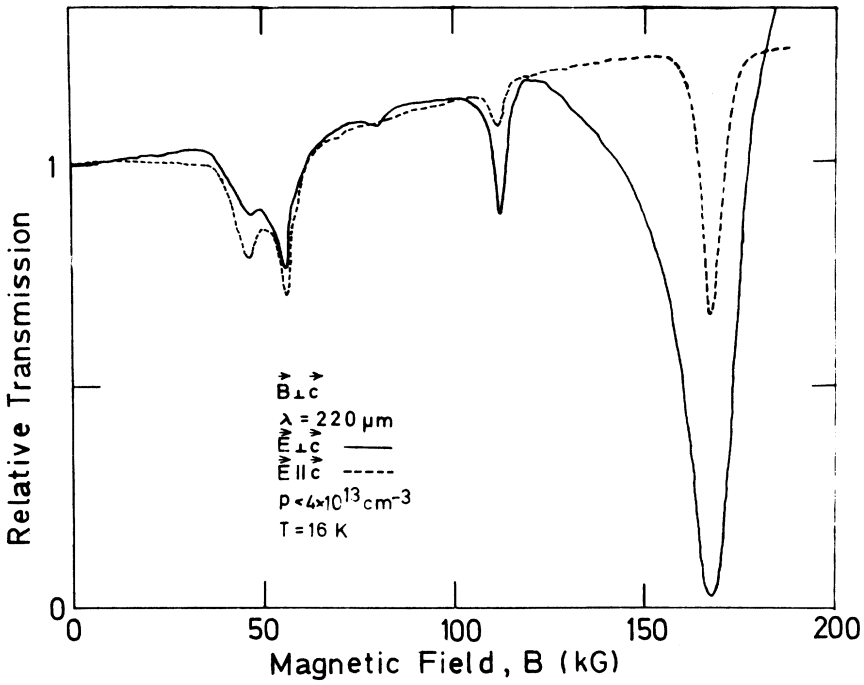


FIG. 6. Experimental data of the relative transmission of 220-$\mu$m wavelength radiation through tellurium as a function of the magnetic field intensity perpendicular to the $c$ axis. The different multi-line spectra for the electric vector polarized perpendicular and parallel to the $c$ axis are plotted by the solid and broken curves, respectively.

millimeter-laser-magneto spectrometer in connection with a 225-kG Bitter-solenoid magnet and has been described already in detail.[17-19] The samples were carefully prepared as described in I. Actually part of the cube-shaped samples were already used in the measurements for the magnectic field parallel to the trigonal axis. Special care was taken to avoid optical interference effects by use of wedged sample surfaces.[20] The incident electromagnetic radiation was linearly polarized better than 99% by a Hertz grid directly in front of the sample. The temperature was measured by use of a calibrated carbon thermometer.

### B. Experimental transmission spectra

In Fig. 6 we have plotted the relative transmission of 220-$\mu$m wavelength radiation through an 0.3 cm thick tellurium sample as a function of the magnetic field intensity perpendicular to the $c$ axis. Although the experimentally controlled field quantity is not the magnetic induction $B$ but the magnetic field $H$, we characterize the magnetic field intensity by $B$ because of its fundamental significance on the energy quantization. Using this notation the relative permeability in tellurium was supposed to be $\mu = 1$. The broken and solid curves in Fig. 6 represent the results for the electric polarization vector parallel and perpendicular to the trigonal axis, respectively. We observe four dominant resonance lines which are indicated by the quantum numbers of the initial and final state.

In addition to these allowed strong transitions, there is an additional weak line at about 80 kG which may be interpreted as the forbidden $0^+$-$1^+$ transition. This transition could possibly be excited by the interactions of phonons or impurities with the quantized charge carriers.

In Fig. 7 we have plotted the corresponding re-

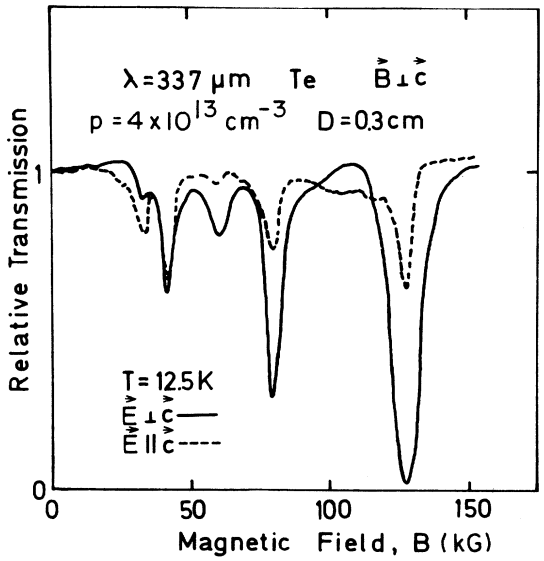


FIG. 7. Due to the smaller energy of the 337-$\mu$m wavelength radiation the resonance lines in the experimental spectra of the relative transmission are shifted to lower magnetic field intensities compared to Fig. 6.

sults for 337-$\mu$m wavelength radiation. Again the four allowed and one forbidden transition are the dominant features of the spectrum. All resonance lines, however, are shifted to lower magnetic field intensities because of the decrease in the radiation energy.

Because of the narrowness of the resonance lines the exact position of the transmission minima in the different spectra could be related to each other with an error of less than 0.2 kG. The absolute error in the magnetic field intensity, however, depends on the field calibration of the solenoid magnet and is in the order of one percent.

### C. Temperature dependence of the resonance lines

We performed an intensity study of the different spectra as a function of the temperature ranging from 5 to 75 K. Special care was taken in the determination of the linewidth and the peak position of the $0^+$-$0^-$ and the $0^-$-$1^+$ transition. To determine the temperature dependence of the damping parameter we have fitted the line shape of the $0^+$-$0^-$ transition and obtained for all models to very good approximation the same functional dependence $\Gamma(T)$ as shown in Fig. 8. With increasing temperature the scattering process becomes stronger and changes the damping parameter to larger values. This experimentally determined fit of the damping parameter $\Gamma(T)$ happens to be independent of both the transition involved and the radiation frequency. This fact is demonstrated in Figs. 9 and 10 where we have plotted the experimentally determined values of the linewidth for the $0^-$-$0^+$ transition for 220- and 337-$\mu$m wavelength radiation, respectively. The solid lines represent the theoretically calculated linewidth of the $0^-$-$1^+$ transition using the temperature-dependent $\Gamma(T)$ of the $0^+$-$0^-$ line as shown in Fig. 9. The excellent agreement of the theoretical and experimental results proves that in tellurium, for $\vec{B}\perp\vec{c}$, the damping parameter $\Gamma$ is independent of the quantum numbers, the magnetic field intensity, and the radiation fre-

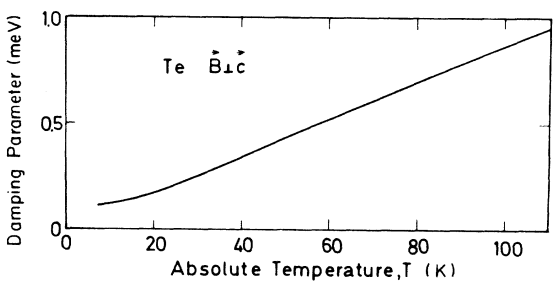


FIG. 8. Damping parameter $\Gamma$ as a function of the temperature was derived from the line-shape fit of the $0^+$-$0^-$ transition.

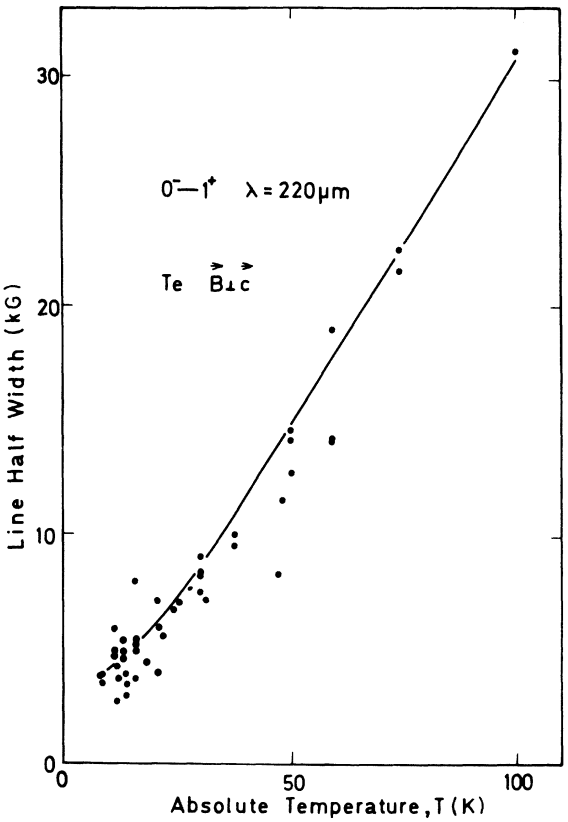


FIG. 9. Experimental data of the half width of the $0^-$-$1^+$ transition using 220-$\mu$m wavelength radiation are represented by dots. The solid curve shows the calculated line half width using the fit values for the damping parameter $\Gamma$ as shown in Fig. 8. The good agreement demonstrates that the damping parameter $\Gamma$ is the same for the $0^+$-$0^-$ and the $0^-$-$1^+$ transition.

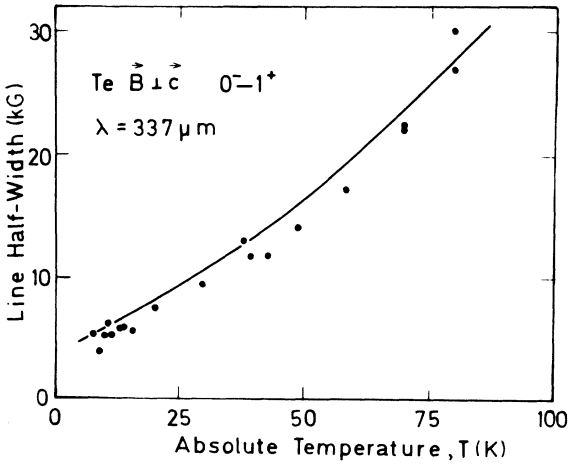


FIG. 10. Good agreement of the experimental (dots) and calculated (solid curve) line half width for 337-$\mu$m wavelength radiation demonstrates that the damping parameter $\Gamma$ is also independent of the radiation frequency.

quency, depending only on the temperature. In this independence of most of the parameters the situation for $\vec{B} \perp \vec{c}$ is similar to the case for $\vec{B} \parallel \vec{c}$. The explicit temperature dependence for $\vec{B} \perp \vec{c}$, however, differs considerably from the temperature dependence of the damping parameter for $\vec{B} \parallel \vec{c}$ as discussed in I.

### D. Comparison of theoretical models with experimental data

In Figs. 11 and 12 the points represent experimental data of the peak positions of the $0^+$-$0^-$ and $0^-$-$1^+$ transition as a function of the temperature for 220-$\mu$m wavelength radiation. The magnetic field intensity of the transmission minima increases monotonically with increasing temperature. In addition to the experimental data we have included the theoretical results as calculated from the four models using different values of the damping parameter $\Gamma$. The temperature dependence of the peak position for constant damping parameter reflects at high temperature the nonparabolicity of the valence-band model involved. In addition to the influence of the nonparabolicity, we have included the effect of the temperature-dependent increase of the damping parameter $\Gamma(T)$ as well. The solid lines correspond to the best fit in the line shape of the theoretical results. All of the models reproduce the general increase of the peak position vs temperature quite well but they differ considerably in the absolute value of the line position. Model C has the least agreement with the experimental situation and deviates in the peak position by about 7%. Model W2 shows the best agreement; the most astonishing fact is that model W2, which has already been ruled out in I, shows the best agreement. This model, however, should not be realistic for such high magnetic field intensities, because of the strong $k^4$ contribution. This fact actually demonstrates a crucial point in physical interpretation: an established model may have excellent agreement with only some aspects of the experimental results and may be ruled out by complementary data. Because of the consistency of theory, such models have to be excluded. Model W1 and J both agree within an error of about 3% with the experimental data. The corresponding results, both experimentally and theoretically,

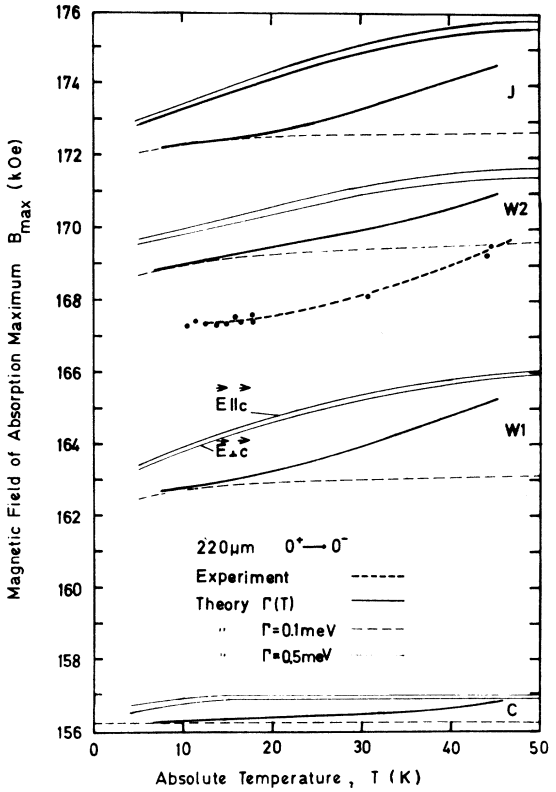


FIG. 11. Comparison of the experimental and theoretical peak position of the $0^+$-$0^-$ transition using 220-$\mu$m wavelength radiation for the models W2 (Ref. 2) and W1 (Ref. 1).

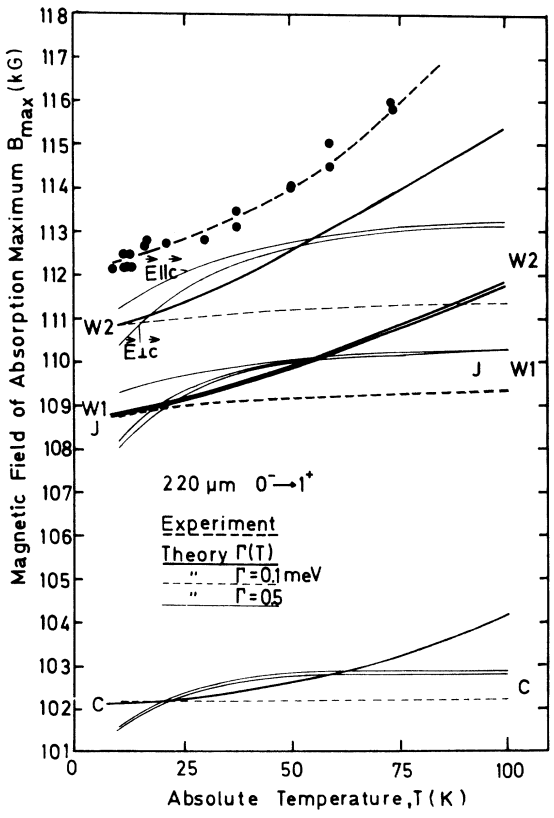


FIG. 12. Whereas the unrealistic model W2 (Ref. 2) reproduces the experimental peak position of the $0^-$-$1^+$ transition of 220-$\mu$m wavelength radiation best, no distinction between model W1 (Ref. 1) and J (Ref. 3) can be made.

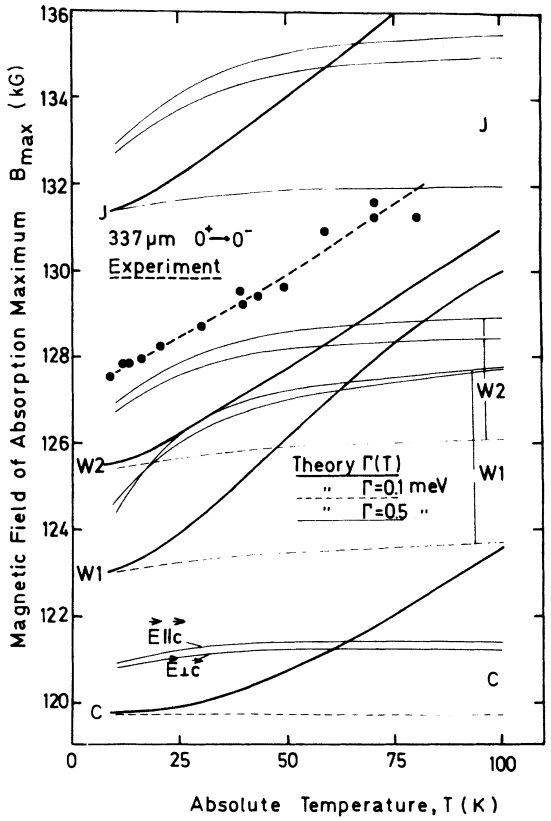


FIG. 13. Experimental peak position as a function of the temperature for the $0^+$-$0^-$ transition induced by 337-$\mu$m wavelength radiation.

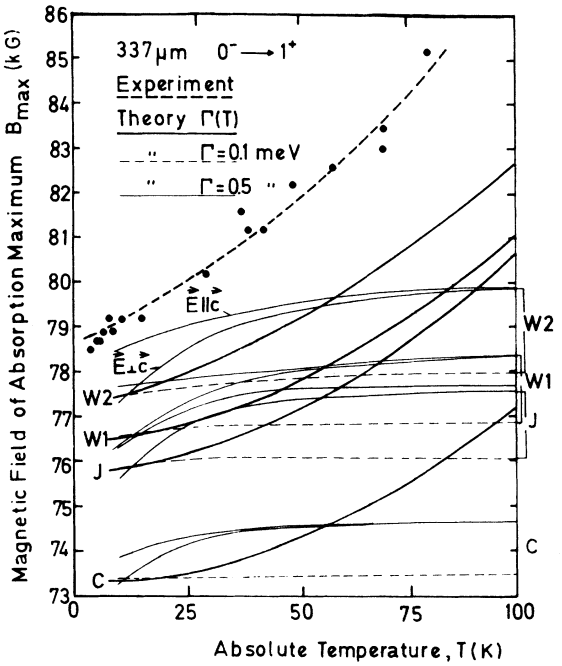


FIG. 14. Comparison of the experimental and theoretical peak position of the $0^- - 1^+$ transition using 337-$\mu$m wavelength radiation favors the unrealistic model W2 (Ref. 2) more than the realistic model W1 (Ref. 1).

for 337-$\mu$m wavelength radiation are plotted in Figs. 13 and 14. Again model W2 seems to show the best agreement and model C the least agreement with the experimental situation. Models J and W1 follow the experimental data at an equal distance.

In contrast to the situation of the magnetic field orientation parallel to the trigonal axis as discussed in I, we find that for $\vec{B} \perp \vec{c}$ there are no characteristic features here in the functional dependence of the peak position vs temperature, which in I provided for $\vec{B} \parallel \vec{c}$ an important criterion to rule out some of the models. Another tool to probe the energy separation between the Landau levels is the investigation of the thermodynamical occupation. By means of the temperature, the occupation probability can be changed. This is reflected in the temperature dependence of the line intensity. For high temperature the occupation probability can be approximated by a Boltzmann function. As long as only two Landau levels are involved therefore, a simple log plot of the line intensity vs reciprocal temperature reveals the energy separation of the two levels considered. In Fig. 15 we demonstrate this method for the $0^-$-$1^+$ transition induced by 337-$\mu$m wavelength radiation. From the slope we derive an energy separation of 1.7 meV, which is in excellent agreement with the theoretical value in model W1. At high temperatures the agreement is less good, because more than two Landau levels are occupied.

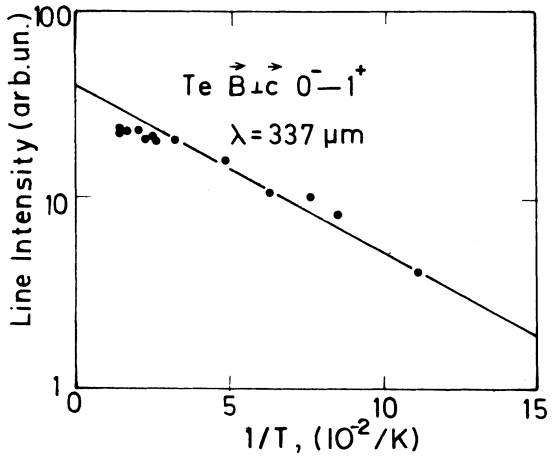


FIG. 15. Temperature dependence of the $0^-$-$1^+$ line intensity is determined by energy separation of the $0^-$ state from the ground state $0^+$. From the slope of the experimental data in this figure a value of 1.7 meV is derived, which is in excellent agreement with theory.

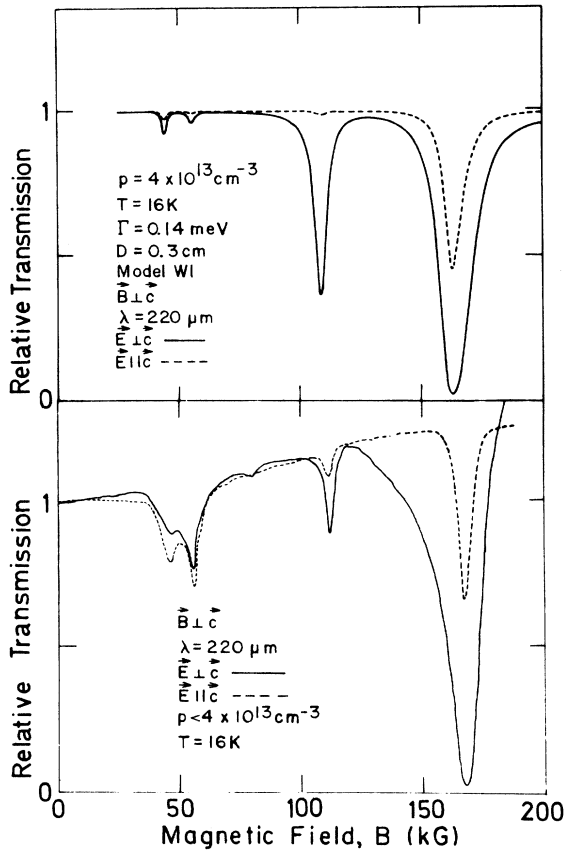


FIG. 16. Direct comparison of the experimental and simulated transmission spectra of 220-$\mu$m wavelength radiation through tellurium in the lower and upper part, respectively, reveals that the absorption intensity of the different transitions is well reproduced by theory only for the $0^+$-$0^-$ resonance.

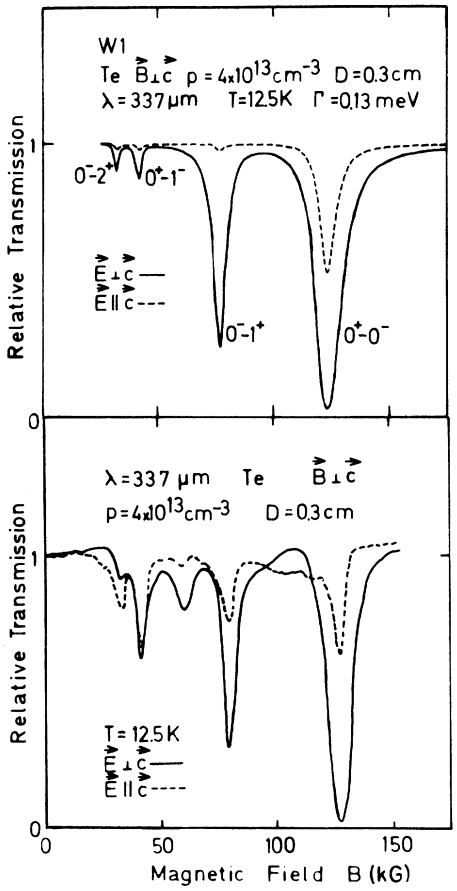


FIG. 17. Experimental transmission spectrum of 337-$\mu$m wavelength radiation through tellurium in the lower part is only well reproduced for the high-field resonance as shown in the simulated spectrum in the upper part of the figure.

### E. Comparison of experimental and simulated transmission spectra

So far we have only compared the experimental data and the four different valence-band models with respect to the energy levels. Additional properties of the wave function as expressed in matrix elements have not yet been considered quantitatively. To include this additional comparison we shall have to analyze the different line intensities in relation to each other. The easiest way to do this is the direct comparison of the simulated transmission spectra and the experimental spectrum of the relative transmission. In Figs. 16 and 17 we present this direct comparison for 220- and 337-$\mu$m wavelength radiation, respectively. We have chosen for this calculation model W1 which is the most realistic model so far as supported by the investigations of I in conjunction with the present study. Models W2, J, and C yield about the same intensities as shown from the theoretical results of the absorption constants. As shown in Figs. 16 and 17, for both wavelengths the intensity of the $0^+$-$0^-$ transition is reproduced rather well theoretically for both of the two different polarization modes. The agreement for the other lines is not as good. The intensity of the $0^-$-$1^+$ transition for the electric field vector parallel to the $c$ axis ($\vec{E} \parallel \vec{c}$) is much too small in comparison to the intensity of the same transition for the electric field vector perpendicular to the $c$ axis ($\vec{E} \perp \vec{c}$). The higher harmonic transitions $0^-$-$2^+$ and $0^+$-$1^-$, too, are much weaker in the theoretical simulation. Whereas the peak position is rather well reproduced by all of the different models, the agreement in the line intensity still leaves something for further theoretical improvement. The difference in agreement for peak position and line intensity is easily understood. All the different theoretical valence-band models are represented by some kind of trial Hamiltonian whose parameters were fitted to the experimental data. It is

well known, however, that any trial Hamiltonian leads to a much better approximation of the energy eigenvalues than of the eigenfunctions. Since the cyclotron-resonance peak position is completely determined by the energy eigenvalues, the theoretical simulation of the resonance position is much less sensitive to a variation of the trial Hamiltonian than the transition intensity which involves the knowledge of two different wave functions.

### F. SUMMARY

We have investigated the cyclotron resonance in tellurium as a function of the temperature for the magnetic field perpendicular to the trigonal axis in the Faraday configuration for both normal modes. The experimental results are compared with the theoretical simulations of the relative transmission curves based on four competing valence-band models. In the theoretical calculations not only temperature and damping effects have been included, but also the explicit nonparabolicity of the states with nonzero wave vector parallel to the magnetic field. Whereas the line position is satisfactorily represented by the different models, the line intensity is only well produced for the $0^+$-$0^-$ transition.

### ACKNOWLEDGMENTS

We wish to express our gratitude to Professor G. Landwehr (Wurzburg) for his interest in this work and stimulating discussions. One of us (M.v.O.) is grateful to the Max Kade Foundation for financial support.

---

*Supported by Max Kade Foundation, New York, N. Y. (Present address: University of Wurzburg, 87 Wurzburg, German Federal Republic).

†Supported by the NSF.

[1]M. H. Weiler, Solid State Commun. 8, 1017 (1970).

[2]W. Dreybrodt, M. H. Weiler, K. J. Button, B. Lax, and G. Landwehr, *Proceedings of the Tenth International Conference on the Physics of Semiconductors, Cambridge, Massachusetts*, 1970 (U.S. AEC, Div. Technical Information, Springfield, Va., 1970) pp. 347–352.

[3]R. Yoshizaki and S. Tanaka, J. Phys. Soc. Jpn. 30, 1389 (1971).

[4]K. Nakao, T. Doi, and H. Kamimura, J. Phys. Soc. Jpn. 30, 1400 (1971).

[5]E. Braun, L. J. Neuringer, and G. Landwehr, Phys. Status Solidi B 53, 635 (1972).

[6]Y. Couder and M. Hulin in *Proceedings of the Eleventh International Conference on the Physics of Semiconductors*, Vol. I (PWN Polish Scientific, Warsaw, 1972), pp. 756–761.

[7]E. Bangert and W. Dreybrodt, Solid State Commun. 10, 623 (1972).

[8]M. v. Ortenberg and K. J. Button, Solid State Commun. 11, 1315 (1972).

[9]M. v. Ortenberg, K. J. Button, G. Landwehr, and D. Fischer, Phys. Rev. B 6, 2100 (1972).

[10]M. v. Ortenberg, K. J. Button, G. Landwehr, and D. Fischer, *Proceedings of the International Conference on the Physics of Semiconductors*, Vol. I, (PWN-Polish Scientific, Warsaw, 1972), pp. 769–775.

[11]M. v. Ortenberg and G. Landwehr, Autumn Meeting of the British Radio Spectroscopy Group, Newcastle-Upon-Tyne, U. K., 1972 (unpublished).

[12]M. v. Ortenberg, K. J. Button, and G. Landwehr, Verhandlungen der DPG, (VI) 8, 350 (1973).

[13]M. v. Ortenberg and R. Ranvaud, Solid State Commun. 13, 333 (1973).

[14]Y. Couder, M. Hulin, and H. Thome, Phys. Rev. B 7, 4373 (1973).

[15]R. Kubo, J. Phys. Soc. Jpn. 12, 570 (1957).

[16]P. Grosse, *Die Festkörpereigenschaften von Tellur* (Springer, Berlin, 1969).

[17]K. J. Button and B. Lax, *Submillimeter Waves* (Polytechnic, New York, 1971), pp. 401–416.

[18]K. J. Button, *Optical Properties of Solids*, edited by E. D. Haidemenakis (Gordon and Breach, New York, 1970), pp. 253–279.

[19]K. J. Button, Laser Focus 7, 29 (1971).

[20]T. L. Cronburg and B. Lax, Phys. Lett. A 37, 135 (1971).